Applied Catalysis B: Environmental 248 (2019) 157–166

Contents lists available at ScienceDirect

Applied Catalysis B: Environmental

journal homepage: www.elsevier.com/locate/apcatb

Size-dependent photocatalytic activity of carbon dots with surface-state determined photoluminescence

Yiqun Zhou[a], Elsayed M. Zahran[b,*], Bruno A. Quiroga[a], Jennifer Perez[a], Keenan J. Mintz[a], Zhili Peng[a], Piumi Y. Liyanage[a], Raja R. Pandey[c], Charles C. Chusuei[c], Roger M. Leblanc[a,*]

[a] Department of Chemistry, University of Miami, Coral Gables, FL, 33146, USA
[b] Department of Chemistry, Ball State University, Muncie, IN, 47306, USA
[c] Department of Chemistry, Middle Tennessee State University, Murfreesboro, TN, 37132, USA

ARTICLE INFO

Keywords:
Photocatalysis
Carbon dots
Organic compound degradation
ROS
Photoluminescence

ABSTRACT

Carbon dots (CDs) were synthesized by a microwave-mediated method and separated by size exclusion chromatography into three different size fractions. There was no correlation of CD size with photoluminescence (PL) emission wavelength, showing that the PL mechanism is not quantum-size dependent. UV/vis absorption and diffuse reflectance spectroscopies showed that the light absorption properties as well as the band gap of the CDs changed with the size of the particle. The combination of FTIR and XPS measurements revealed the composition on the surface of each fraction. The three CDs fractions were separately used in the photocatalytic degradation of organic dyes under simulated sunlight irradiation. The catalytic activity of the as-prepared CDs was found to increase as the size of the particles decreased. Complete degradation of both rhodamine B (RhB) and methylene blue (MB) was achieved in 150 min by the 2-nm CDs. The scavenger studies showed that the holes and superoxide radicals are the main species involved in the photocatalytic degradation of the dye by the 2-nm CDs. These CDs displayed high stability in the degradation of organic dyes for multiple cycles. The 2-nm CDs displayed promising photocatalytic degradation of p-nitrophenol (PNP). These results demonstrate for the first time the application of bare carbon dots in the degradation of environmental contaminants.

1. Introduction

Environmental protection and energy crisis are two critical issues brought by the rapid growth of population and increasing daily demand. To avoid the implications of these issues, while considering the sustainability in the development, new resources are being widely explored such as solar energy. For this, photoactive materials are drawing much attention due to the unlimited sunlight energy and potential application as a catalyst for hydrogen generation via water splitting and for pollutants degradation [1,2]. Since hydrogen is considered as a renewable and sustainable energy resource, photocatalysis has become one promising solution to solve both issues.

Since the discovery of TiO_2 as a photocatalyst by Honda and Fujishima in 1972, in the past 40 years [3], much effort has been devoted to developing photocatalysts that act efficiently under visible light irradiation. To date, there are varieties of photocatalyst including metal oxides such as TiO_2 [4], Fe_2O_3 [5], ZnO [6], ZnS [7], $BiVO_4$ [8], metal chalcogenides, for example, CdS and MoS_2 [9], and nitrides, especially graphitic carbon nitrides [10]. However, the majority of photocatalysts contain metals, which poses a risk of secondary pollution to water bodies after the degradation of the contaminants. In addition, sulfides are not stable and photocorrosion is easy to occur [11]. Even though oxides are stable in aqueous solution and low cost, most of them usually possess large band gap [12]. Therefore, the development of nontoxic, stable and efficient photocatalysts is desirable for applications such as the photocatalytic water splitting and the photocatalytic degradation of pollutant.

Carbon dots (CDs), as a new family member of carbon-based nanomaterials, have been widely synthesized with various methods, such as pyrolysis within autoclave [13], hydrothermal/solvothermal reaction with refluxing [14], fast microwave-assisted synthesis [15], laser ablation [16], and ultrasonication with high frequency [17]. Due to their ultra-small size, this class of nanomaterials exhibits unique properties that are distinctively different from their bulk counterparts. Because of their high photoluminescence (PL), good biocompatibility, water dispersity, low toxicity, abundant electron donors and acceptors, and controlled surface states [18], CDs are becoming promising materials in various fields including engineering [19], drug delivery [20,21],

* Corresponding authors.
E-mail address: rml@miami.edu (R.M. Leblanc).

https://doi.org/10.1016/j.apcatb.2019.02.019
Received 14 December 2018; Received in revised form 30 January 2019; Accepted 9 February 2019
Available online 11 February 2019
0926-3373/

bioimaging [22,23], sensing [24,25], catalysis [26], and energy conversion and storage [27–29].

In addition, carbon dots exhibit tunable fluorescent quantum yield (QY) based on starting precursors [30], preparation methods [31], and post-treatment [16]. For instance, the highest QY value to date has reached 93.3% when CDs were prepared with citric and tris-(hydroxymethyl)aminomethane (Tris) through a microwave-mediated route [32]. Besides the success in the enhancement of QY, the mechanism of the PL of CDs is one of the most disputed topics [33]. The explanation of the mechanism resonates among two main causes, namely the size effect and the surface state [34], which is inspired by traditional quantum dots even though the size effect is not often used to explain the PL mechanism of CDs. The surface state comprises of the functional groups on the surface of CDs nanoparticles as well as the energy traps, which determine the emission of CDs by the generation and transition of excitons [35]. Considering CDs are semiconductors, the excitons generate electrons and holes [36]. When CDs are excited, the electrons in the valence band transit to the conduction band. By vibrational relaxation, the electrons will move to the energy levels caused by surface states of CDs. However, the introduction of oxygen and nitrogen elements and related chemical bonds will produce impurity levels in the surface states, which leads to the narrowing of the band gap between the surface states and valence band [37]. Consequently, fluorescence emission is generated along the electrons transition from these energy levels to the valence band. Due to the single or multiple band gaps between the valence band and surface states, the emission exhibits uniform or various PL wavelengths, which explains why some CDs exhibit excitation wavelength-independent or -dependent PL [38]. This whole process is illustrated in Scheme 1.

Since CDs are photoluminescent semiconductors with a specific energy band gap between the valence and conduction bands [39], they have the potential to drive photocatalytic redox reactions. For instance, these properties make CDs a good candidate for photocatalytic water splitting into hydrogen and oxygen [40]. Furthermore, the photocatalytic redox activity of CDs has been utilized *in vivo* to generate reactive oxygen species (ROS) to cause the death of hypoxic tumor cells [41]. However, although photocatalytic water splitting is promising for hydrogen generation and photodynamic therapy, it has been a challenge to design photocatalysts with efficient solar to hydrogen conversion due to the recombination of the electron/hole pairs and the fast backward reactions [42]. In addition, most traditional photocatalysts, such as TiO_2 and ZnO can only utilize UV light with band gaps greater than 3.0 eV [3]. Therefore, the development of stable photocatalyst that absorb in the visible light with narrow band gap is very much sought. Carbon-based materials such as graphitic carbon nitride (g-C_3N_4) has emerged as a promising photocatalyst with a band gap of 2.7 eV that is situated for visible light reactions [43]. Therefore, considering the similar polymeric structure of CDs as g-C_3N_4, and the abundant electron donors and acceptors on CDs, the photocatalytic properties of CDs should be investigated. Recently, CDs have been integrated in heterostructures to enhance the activity of various photocatalysts [44,45] and they are able to play manifold roles in heterogeneous photocatalysis. For example, they are photoelectron mediator and acceptor, photosensitizer, reducing agent, and they can enhance adsorption capacity [46,47]. Furthermore, there are many advantages that facilitate the application of CDs as photocatalyst. First, they are well-dispersed in water, which yields a homogeneous phase to efficiently absorb water on their surface [48]. Additionally, CDs are non-toxic, they will not contaminate the body of water or have adverse effect on the human health. However, even though CDs have been utilized to enhance the photocatalytic activity of various metal oxide nanomaterials such as Fe_2O_3 [49], TiO_2 [50], ZnO [51], SnS_2 [52], and BiOBr [53]. There are fewer studies on the photocatalytic properties of bare CDs, especially on the photocatalytic dye degradation [54]. Otherwise, the photocatalytic activity of bare CDs is usually negligible [55].

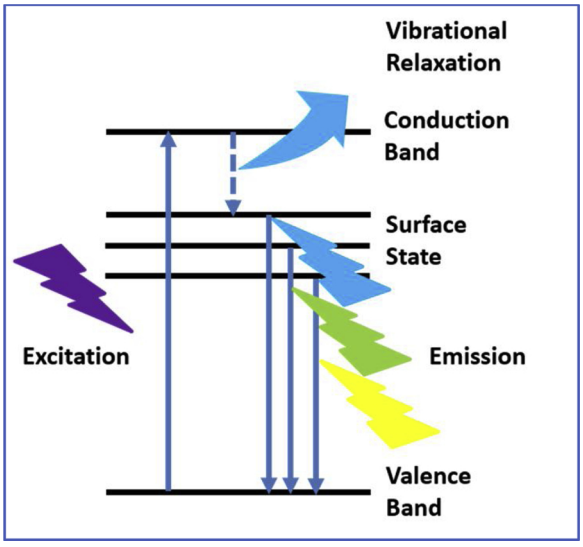

Scheme 1. The illustration of electron transition of CDs upon excitation.

Herein, in this study, we focus on the photocatalytic activity of the bare CDs as well as the influence of size on the photocatalytic performance. CDs were synthesized via a microwave-assisted reaction of citric acid as carbon precursor and 1,2-phenylenediamine as the nitrogen dopant. After purification by size exclusion chromatography, we obtained three CDs fractions with different sizes. These CDs demonstrated size dependent photocatalytic activity in the degradation of organic dyes. The mechanism of the dye degradation was analyzed using various charge-carrier scavengers from the viewpoint of generation of superoxide and hydroxide radicals. The stability test was conducted to reveal the effectiveness of CDs in the long term of dye degradation. The CDs were employed in the photocatalytic degradation of, p-nitrophenol (PNP), one of the most hazardous refractory pollutants with high stability and solubility in water [56], to demonstrate their application for various environmental contaminates.

2. Experimental

2.1. Materials

Citric acid (99.5–100%) was purchased from VWR (West Chester, PA, USA). Also, 1,2-phenylenediamine flakes (99.5%), rhodamine B (RhB), methylene blue (MB) and IPA (isopropanol alcohol) were obtained from Sigma-Aldrich (St. Louis, MO, USA). Benzoquinone (98 + %) and p-nitrophenol (PNP) (99%) were bought from Alfa Aesar (Haverhill, MA, USA). EDTA (disodium ethylenediaminetetraacetic acid) was procured from J.T. Baker Chemical Co. (Phillipsburg, NJ, USA). The distilled water used was purified using a Modulab 2020 water purification system acquired from Continental Water System Corporation (San Antonio, TX, USA). The water had a pH of 6.62 ± 0.3 at 25 ± 0.5 °C with a resistivity of 18 MΩ cm and surface tension of 72.6 mN m^{-1}. The SEC was performed using GE Healthcare Sephacryl S-300 (Uppsala, Sweden) as the matrix. The Whatman® qualitative filter paper, Grade 3 (diameter: 70 mm) were bought from GE Healthcare Life Sciences. Argon gas was bought from Airgas (Miami, FL, USA). All chemicals were used without further treatment.

2.2. Methods

The UV/Vis absorption spectra of three CD fractions were obtained using a Cary 100 UV/Vis spectrophotometer and a 1 cm optical cell. A Fluorolog (Horiba Jobin Yvon) spectrometer was used to record the fluorescence emission spectra of sample with a slit width of 5 nm used for both excitation and emission. As for the determination of

fluorescence quantum yield, a Varian Cary Eclipse spectrometer was used to record the fluorescence spectra of samples and standards. Fourier-transform infrared (FTIR) spectroscopy data were obtained with a Perkin Elmer FTIR (Frontier) spectrometer by using the attenuated total reflection (ATR) technique with air as background. XPS data was acquired using a Perkin Elmer PHI 560 system with a double-pass cylindrical mirror analyzer operated using a Mg Kα anode with a hυ = 1253.6 eV photon energy operated at 250 W and 13 kV. Zeta potential measurements were made by using a nano series Malvern Zetasizer. AFM images were obtained with an Agilent 5420 atomic force microscope in the tapping mode. TEM was performed using a JEOL 1200X TEM.

2.3. Synthesis and purification of CDs

To prepare the long emission wavelength CDs, 0.02 g citric acid and 0.28 g 1,2-phenylenediamine were dissolved in 10 mL deionized H_2O. Subsequently, the mixture was placed in a crucible and heated in a microwave oven for 7 min under 700 W until all the water was evaporated. The remaining black powder was dispersed in deionized water and the solution exhibited blue PL under UV lamp. After purification by filtration and SEC, three photoluminescent eluents were collected, which indicated three CDs fractions. The synthesis of CDs and three CDs fractions are shown in Fig. 1a and b, respectively.

2.4. Photocatalytic evaluation of CDs

First, 3 mg of each CDs fraction was mixed with 200 μL RhB (10 mg/L) aqueous solution and 3.8 mL deionized water in a 4-mL UV/vis cuvette. After 2-min of ultrasonication to completely disperse CDs fraction in deionized water, the cuvette was placed in front of a solar simulator (Oriel Instruments, Newport Corporation) with high power mercury-xenon light source (310 W) with vigorous stirring at 200 rpm. Similar procedure was implemented with MB and PNP. However, in order to keep the UV/vis absorption below 1 to have a high light transmittance, the amount of MB was readjusted. After the pilot experiment, 3 mg of each CDs fraction was mixed with 1 mL MB (10 mg/L) aqueous solution and 3 mL deionized water. The rest of the procedure remained the same. Then the UV/vis spectroscopy was performed on the aqueous solutions of dyes (RhB or MB) and CDs fractions (1, 2 or 3). The UV/vis absorption of the reaction was recorded at every 10-min of irradiation. For PNP degradation, 3 mg of CDs fraction 3 was mixed with 1 mL (0.02 g/L) PNP aqueous solution and 3 mL deionized water. This very same procedure was repeated as needed.

3. Results and discussion

3.1. Characterization

Various techniques were applied to reveal the optical, structural, morphological, and electric properties of CDs. UV/vis absorption spectrophotometry was applied to illustrate the conjugated structures including C = C, C = N, and C = O. In Fig. S1a, we can observe peaks at 242, 272 and 324 nm for C = C, C = N, and C = O, respectively in fraction 1 [57,58]. Additionally, there is a peak at 390 nm in the lower-energy region, which might be attributed to the absorption cross section of NO_2 [59]. In Fig. S1b, we can observe peaks at 258, 280 and 323 nm for C = C, C = N, and C = O, respectively, in fraction 2. However, the peak in the lower-energy region was shifted to longer wavelength (417 nm), which could be ascribed to longer conjugated structures. In Fig. S1c shows peaks for C = C (250 nm), C = N (271 nm), C = O (341 nm) in fraction 3 and a similar peak in the lower-energy region at 417 nm.

The fluorescence emission spectra recorded the versatile PL behaviors of three CDs fractions. From the spectrum in Fig. 2a, we can observe that the emission of fraction 1 is independent of excitation wavelength. In addition, the maximum excitation and emission wavelengths of fraction 1 is 375 and 438 nm, respectively, which explains the blue PL as shown in Fig. 1b. In Fig. 2b, the emission is also excitation-independent, and the maximum excitation and emission wavelengths are 400 and 565 nm, respectively, which confirms the yellow PL of fraction 2. On the other hand, fraction 3 (Fig. 2c) displayed more than one emission peaks. For instance, when excited at 350 nm, fraction 3 shows emission peaks at 370, 391, and 414 nm. These peaks are excitation-dependent, which is a typical feature of CDs. However, since the wavelength of excitation is 365 nm (Fig. 1b), the emission wavelength is around 500 nm, which corresponds to green PL that was observed. Surface state-controlled PL is commonly attributed to the origin of CDs' PL. Based on the excitation independent nature of fractions 1 and 2, we expect they should possess a uniform and defect free surface state. Based on the excitation dependent PL of fraction 3, we hypothesize there might be an abundance of defects in the atomic lattice of CDs, which causes the excitation dependence and the random trend of PL color in fractions 1–3, which has been confirmed later by XPS measurements. Accordingly, the fluorescence quantum yield (QY) of fractions 1, 2 and 3 were calculated according to Equation S1 to be 39.2%, 4.3%, and 5.1 %, respectively. The QY of fraction 1 and 3 was measured with quinine sulfate dissolved in 0.05 M H_2SO_4 aqueous solution as standard solution with the QY of 55%. However, according to the degree of overlap in the emission spectra of standard solution and sample, fraction 2 was measured with tris(bipyridine)ruthenium (II) chloride in H_2O as the standard solution with the QY of 2.8%. In

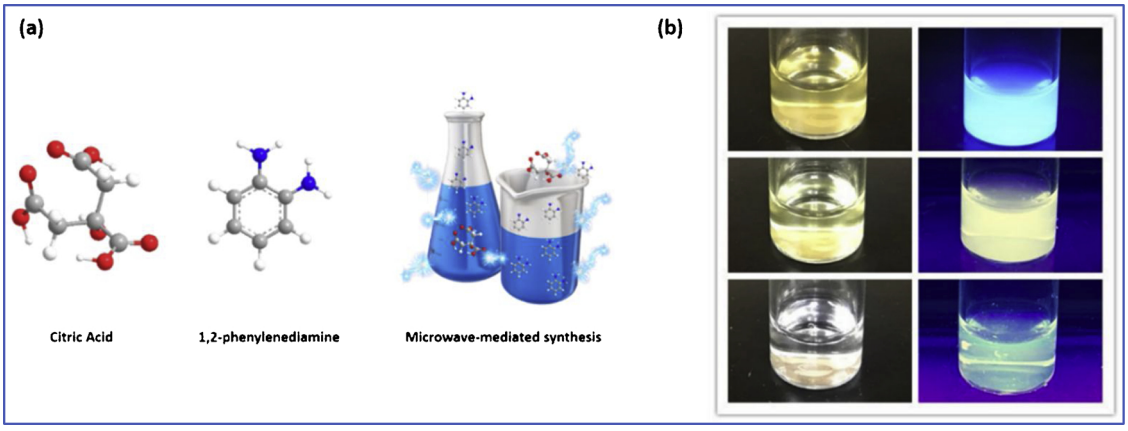

Fig. 1. (a) The precursors and microwave-mediated synthesis of CDs. (b) The aqueous solutions of three CDs fractions with a concentration of 0.1 mg/mL (top-down: fraction 1, 2 and 3) after purification. (The left column is under regular light; the right column is under the UV light at 365 nm).

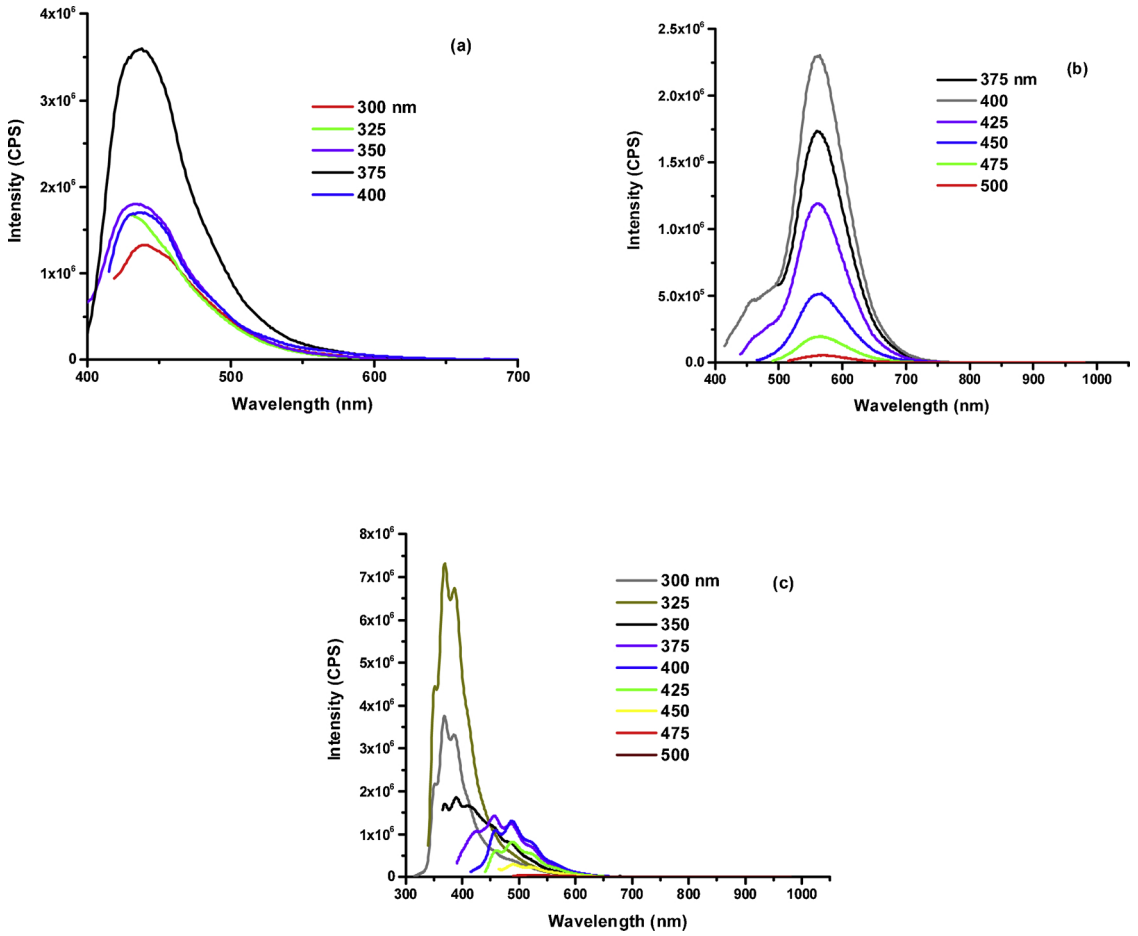

Fig. 2. The fluorescence spectra of fraction 1 (a), 2 (b) and 3 (c). The concentration of fraction 1, 2 and 3 is 0.00019_2, 0.056 and 0.25 mg/mL, respectively.

comparison to fraction 1, the lower QY of fraction 2 and 3 might result from the aggregation-caused quenching [60], which is indicated by the low zeta potential values of 17.2 and 10.7 mV for fraction 2 and 3, respectively. The absolute value of zeta potential decreases from 20.5 for fraction 1 to 10.7 mV for fraction 3, which indicates the tendency of aggregation increases as the size of the CD decreases.

ATR-FTIR measurements were conducted to analyze the functional groups of the three fractions. As displayed in Fig. 3, all the three fractions have N—H or O—H (3341-3058 cm^{-1}), C═C or C═N (1635 cm^{-1}) and C═O (1896 cm^{-1}) groups. This suggests that the three fractions are similar regarding the chemical composition. This is consistent with UV/vis absorption spectra results in Fig. S1 that show the presence of C═C, C═N and C═O in the conjugated structures. Note that the N—H and O—H groups enhance the water dispersity of the CDs. Nonetheless, the stability of fraction 3 colloidal solution is better than that of fraction 2, while fraction 2 is better than fraction 1. This observation could be explained by the carbonization degree of fraction 1 > fraction 2 > fraction 3, which is demonstrated by the C content shown in Table S1 in the supporting information. Therefore, even though the three fractions share similar functional groups, the surface states and properties may vary depending on the relative abundance of each functional group and the elemental composition at the top-most (~100 Å) surface layers.

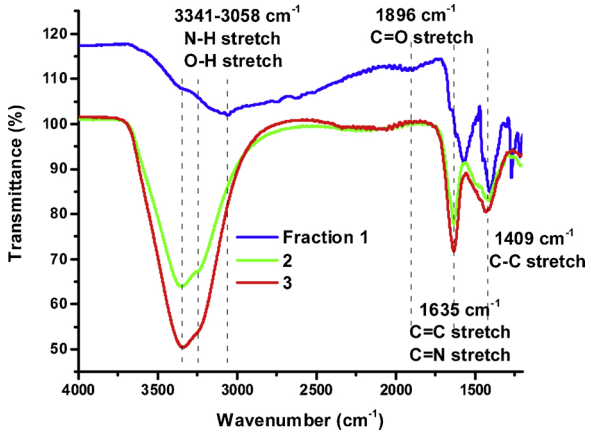

Fig. 3. The FTIR spectra of fraction 1, 2 and 3 in solid state with air as background.

To corroborate this theory, we conducted XPS analysis to study the surface composition of each CDs fraction. Atom mole fraction results (with fwhm and % deconvoluted peak areas in parentheses) are summarized in Table S1 in the supporting information. Fig. 4 shows the XPS stackplots for the C 1 s, N 1 s and O 1 s core levels of the CDs fractions 1 (a), 2 (b), and 3 (c). The C 1 s core level BE at 288.3 eV observed in all fractions denoted carboxylic acid [61]. The O—H and C═O groups have been elucidated by the FTIR (Fig. 3) and UV/Vis absorption (Fig. S1) spectra. There was no noticeable trend in compositional change in the C 1 s levels between various fractions. The N 1 s core levels for all samples show a BE peak center at 399.1 eV consistent with an imine (C═N) group within a ring system [62], which was confirmed by the UV/vis spectra (Fig. S1) and FTIR spectra (Fig. 3). Noteworthy is the fact that there are two observable O 1 s oxidation states that varied in relative quantity between the fractions. The O 1 s core levels for all fractions show BE peak centers at 530.9 and 532.7 eV, consistent with acetate-like O atoms [63], and an O-containing polymeric structure [64], respectively. This result matches the C═O revealed in the FTIR data.

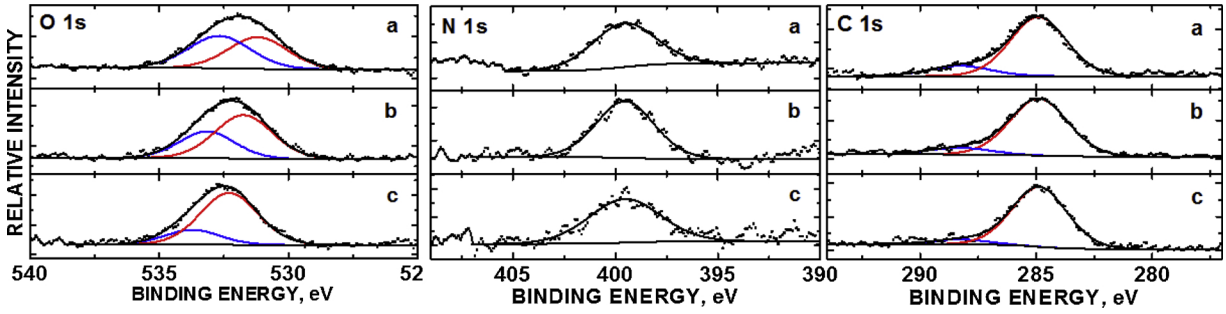

Fig. 4. XPS core levels of O 1 s, N 1 s and C 1 s orbitals of fraction 1 (a), fraction 2 (b), and fraction 3 (c), of the CDs.

From integrated XPS peak area analysis of the deconvoluted oxidation states (Table S1 in the supporting information) in, the following self-consistent trends were observed. The lower O 1 s BE state decreased in the descending order: a (48.4%) > b (27.5%) > c (12.5%). Simultaneously, a decrease in overall atomic % N was observed in the descending order: a (1.6%) > b (1.0%) > c (0.7%). A decrease in overall atomic % C was observed in the descending order: a (87.1%) > b (78.5%) > c (66.1%). There was also a decrease in the amide −COOH oxidation state as denoted in the relative integrated peak areas in the C 1 s level at BE = 288.3 eV in the descending order: a (16.0%) > b (11.1%) > c (7.8%).

As observed from the AFM images (Fig. 5), the three fractions exhibited different sizes as we previously expected from the CDs separation through the SEC. The size of fraction 1, 2, and 3 is estimated to be around 5, 3 and 2 nm, respectively, according to Fig. 5a, b and c). The average particle size of each fraction has been confirmed by the TEM images shown in Fig. 5d, e and f. From the histograms of TEM images, we observe the sizes of fractions 1, 2 and 3 to be 4.48 ± 1.38, 3.61 ± 0.92 and 2.24 ± 0.45 nm, respectively. The combination of AFM and TEM data revealed typical spherical CD morphology with narrow size distributions. In addition, the random PL color of CD fractions in a size gradient revealed that the quantum size effect is not controlling the PL mechanism of these CD fractions. This is consistent with CDs reported by Cao et al., [65].

3.2. Photocatalytic dye degradation

In order to explore the photocatalytic activity of the as-prepared CDs, considering the negative zeta potential of CDs fractions, positively-charged organic dyes were selected for photocatalytic dye degradation. Therefore, the degradation of RhB and MB was conducted in presence of 0.75 mg/mL of CDs under simulated sunlight. Neither RhB or MB was degraded in the presence of fraction 1 (Fig. S2a and b). As the size of CDs decrease to 3 nm in fraction 2, partial degradation of MB was noticed only in the first 20 min (Fig. S2d). On the other hand, no significant degradation of RhB was found for reactions catalyzed with fraction 2 (Fig. S2c). On the contrary, the 2-nm CDs of fraction 3 demonstrated significant degradation of RhB and MB, which was both completed in 150 min (Fig. S2e and f). As presented in Fig. 6a, fraction 3 exhibited substantial photocatalytic activity in the degradation of both RhB and MB. Within 60 min, RhB and MB naturally degraded by 20 and 60%, respectively. With the addition of fraction 3, at the same time, the degradation of both dyes was observed at dye absorption peaks at 554 and 664 nm to increase up to 50 and 90%, respectively. The pseudo-first order reaction rate constants were 1.3×10^{-2} and $3.6 \times 10^{-2}\,min^{-1}$, which exhibited the excellent photocatalytic activity in contrast to most previously reported bare carbon dots. For instance, Yang et al. showed CDs/TNS and CDs/P25 composites showed enhanced photocatalytic activity in the degradation of RhB, but there was no dye degradation in the presence of CDs alone [66]. Furthermore, Huang et al. mentioned the reaction rate constant for their nitrogen-doped CDs was 5.1×10^{-4} min^{-1} while for TiO_2, a widely used photocatalyst, it was 1.5×10^{-2} min^{-1} [67]. It suggests the obtained bare CDs with smallest size could be considered as a promising alternative for the common photocatalyst to achieve homogeneous photocatalysis. In addition, in order to illustrate the importance of surface modification to CDs in terms of photocatalysis, Kang et al. compared the CDs and N-doped CDs in the degradation of methyl orange (MO) (a negatively charge dye model) [17]. As a result, 90% MO degraded within 120 min, which benefited from the presence of N-doped CDs. In comparison, bare CDs exhibited lower efficiency, and the 30% MO degradation only occurred within 120 min. Compared to Kang et al.'s [17] N-doped CDs, even though the efficiency of our CD fraction 3 is similar, there was no need of further surface modification, showing the advantages of our CD fraction 3 synthesis method. Additionally, the wavelength-dependent activity of fraction 3 was conducted with a UV cut off filter (λ < 420 nm). As displayed in Fig. 6b the rate of RhB degradation decreased ($k = 2.5 \times 10^{-3}\,min^{-1}$) compared to the one without filter ($k = 1.3 \times 10^{-2}\,min^{-1}$). This comparison demonstrates that the photocatalytic activity of the as-prepared CDs is driven by visible light.

The significant difference in the activity among various CDs fractions as well as fraction 3 in the presence and absence of filter can be explained in light of band gap energy exhibited by each material as measured by diffuse reflectance spectroscopy (Fig. 7). As displayed in Fig. S3, no semiconductor properties were noticed for fraction 1. On the other hand, band gap energies were calculated for fraction 2 and 3 from the spectra in Fig. 7a and b to be 2.36 and 2.04 eV, respectively. Just as revealed by the XPS, fraction 3 has higher content of O in terms of overall atoms, which might introduce more impurity levels in the band gap [37], and result in the narrow band gap of fraction 3. Also, the band gap of fraction 3 is 2.04 eV, which reveals the absorption band edge at around 550 nm, confirming the photocatalytic capability of fraction 3 under the visible light irradiation. According to these values, the as-prepared CDs of Fraction 2 and 3 can be considered as direct semiconductors with narrow band gap that is well-suited for homogeneous photocatalytic degradation reactions. In addition, based on the ratio of C and O overall atomic content of each fraction (F1, 8:1; F2, 4:1, F3, 2:1), it is hypothesized that the stability of the C–O bond has the following order (F3 < F2 < F1), which contributes to the higher photoactivity of fractions 2 and 3.

To further investigate this hypothesis and probe the reaction mechanism, the photocatalytic degradation of RhB and MB by CDs (fraction 3) was conducted in presence of various charged radical scavengers and analyzed with the pseudo-first order reaction rate constant obtained from the RhB absorption peak at 554 nm.

First the photocatalytic degradation of RhB was conducted in presence of EDTA to scavenge the holes. It is generally accepted that photocatalytic reactions are initiated by photochemically generated electrons (e^-) and holes (h^+) [68]. As it is observed from Fig. S4, RhB and MB, especially RhB, have little degradation in the natural state. However, Fig. 8 and S5a showed significant decrease of the dye degradation rate constant in presence of EDTA indicating the mechanism of oxidization of the organic dyes by the holes.

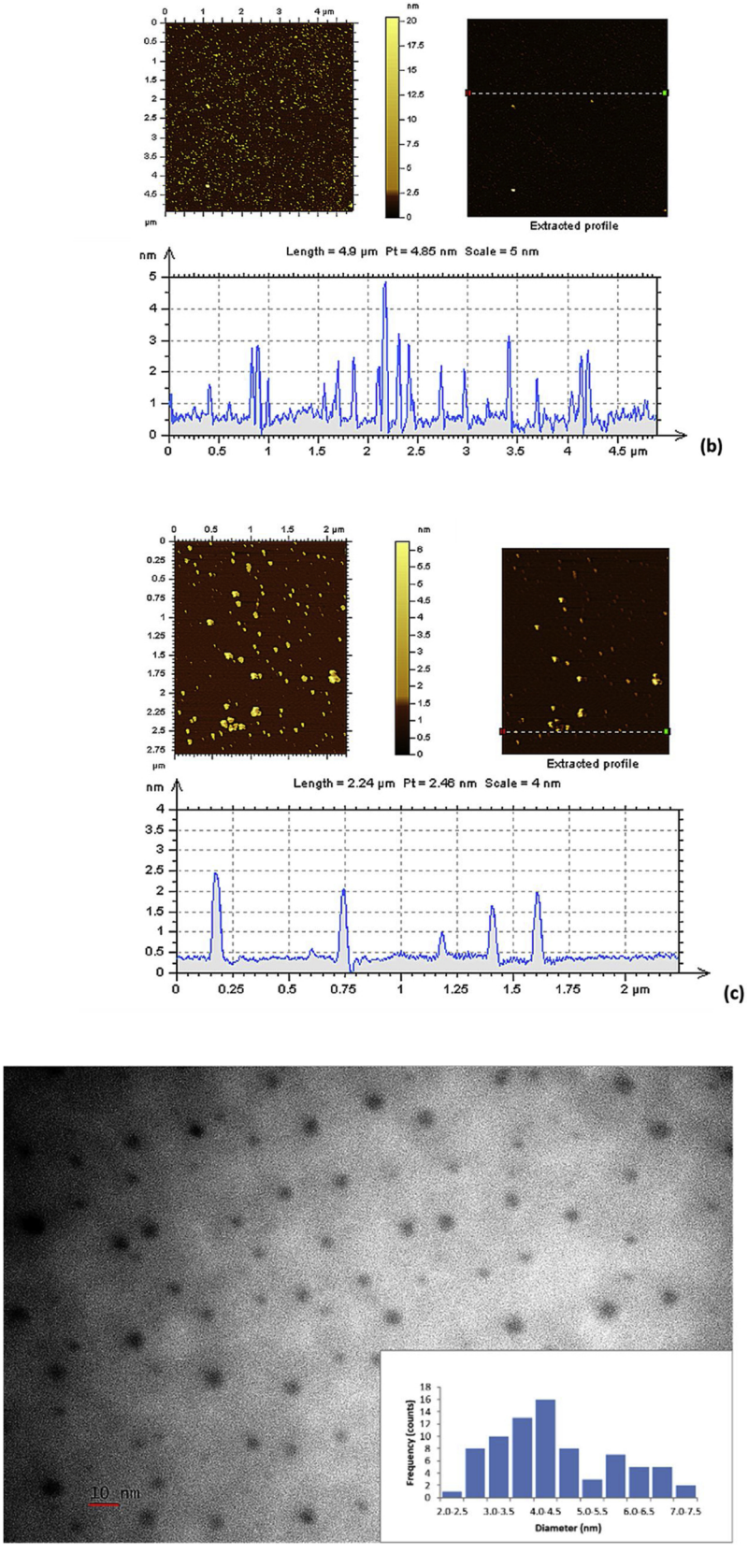

Fig. 5. The AFM images of fraction 1 (a), 2 (b) and 3 (c); the TEM images of fraction 1 (d), 2 (e) and 3 (f). The scale bars represent 10 nm..

In addition, the second mechanism is the generation of ROS (reactive oxygen species) such as superoxide anions and hydroxyl radicals. To examine the presence of such species, benzoquinone (BQ) and isopropyl alcohol (IPA) that had been verified as excellent scavengers [68,69], were employed to scavenge $^{\cdot}O_2^-$ and $^{\cdot}OH$, respectively. The comparison in Fig. 8 and S5, demonstrates that the addition of BQ

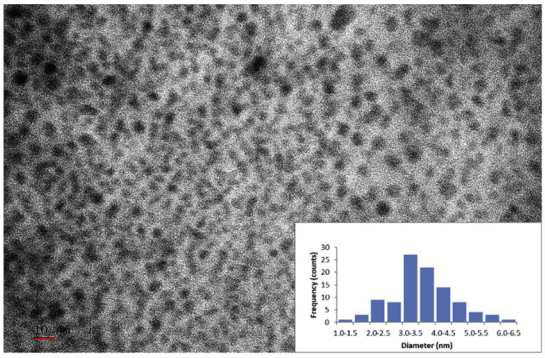

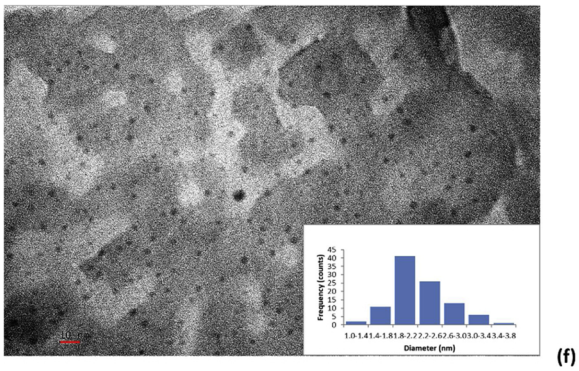

Fig. 5. (*continued*)

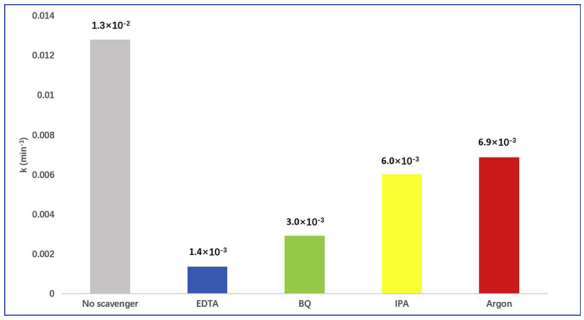

Fig. 8. Photocatalytic degradation rate constants of RhB in the presence of EDTA, BQ, IPA, argon and no scavenger by fraction 3.

significantly inhibited the photocatalytic degradation of RhB. This indicates that electrons from the conduction band of the CDs are donated to the dissolved molecular oxygen to generate $\bullet O_2^-$, which oxidize the RhB. On the other hand, no appreciable change was noticed in the degradation rate of RhB in presence of IPA, which indicates that the oxidation of water by the hole is not impossible. To further elucidate this hypothesis, we used argon gas to flush away oxygen originally dissolved in water for 1 h and insulate the system from oxygen from the environment by using a balloon filled with argon gas. The dye degradation was inhibited compared with the aerobic reaction, which suggested the oxygen dissolved in water also played a certain role in the dye degradation. Another external factor that should be considered is the electrostatic adsorption of dyes onto CDs. Therefore, the adsorption of RhB was performed in dark and the results are recorded in the UV/vis

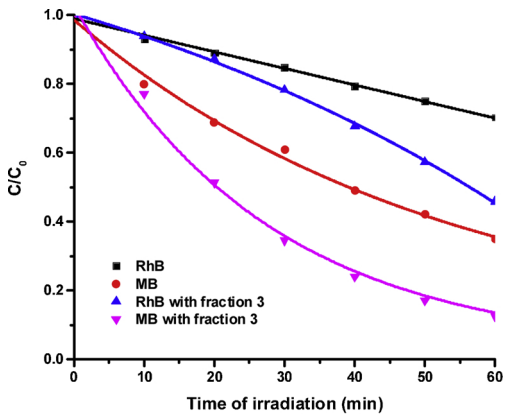

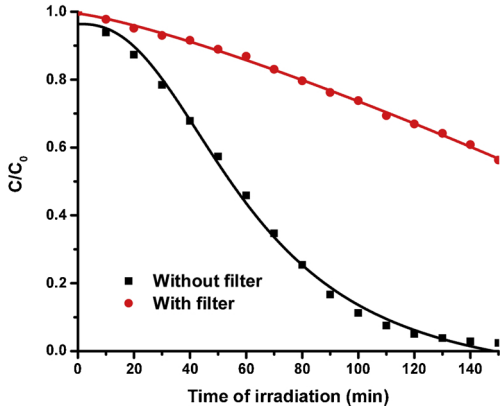

Fig. 6. (a) Photocatalytic degradation of RhB and MB as a function of irradiation time; (b) Wavelength-dependent activity test of fraction 3 in the RhB degradation w/o filter. The concentration of fraction 3 is 0.75 mg/mL.

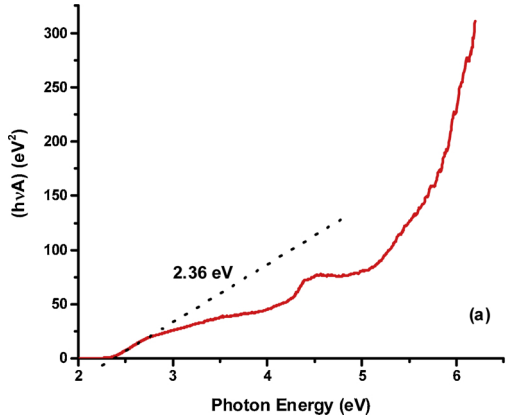

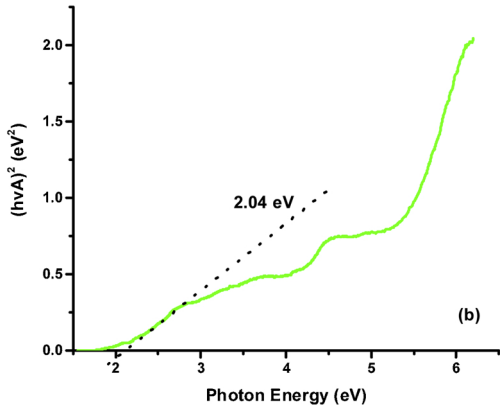

Fig. 7. Diffuse reflectance spectroscopy measurement. Plot of $(\alpha h\upsilon)^2$ vs. photon energy for all the three CDs fractions. F2 (a) and F3 (b).

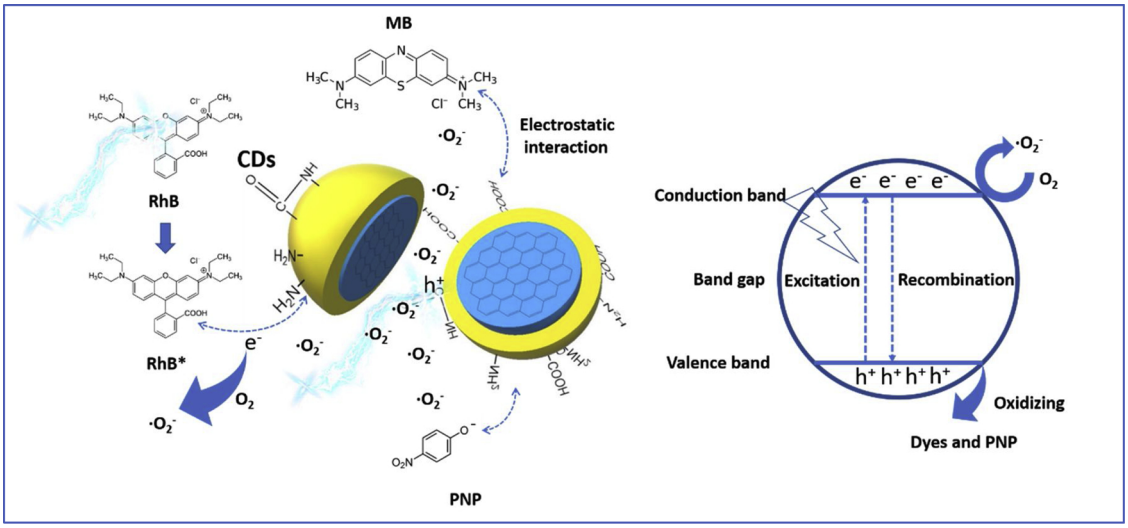

Fig. 9. Schematic diagram of the interaction between CDs and dyes in the photocatalytic dye degradation.

spectrum in Fig. S6. It was noticed that the absorbance of RhB slightly increased in the first 20 min due to the stirring-initiated desorption. However, after 20 min, no remarkable change in the absorbance was noticed until 60 min. This indicates minimal effects of the electrostatic adsorption on the degradation of the organic compounds. Furthermore, was found that RhB molecules can also be excited under visible light irradiation to form RhB* radicals [70]. In this case, radicals can be adsorbed onto the surface of CDs and transfer electrons from/to the conduction/valence bands. In addition, electrons can activate O_2 to form $^{\cdot}O_2$–, which also enhances RhB degradation and overall photocatalytic efficiency of the CDs. Thus, the RhB degradation mechanism might not be only dependent on the holes and superoxide radical anions generated at the valence and conduction bands, respectively, but also related to the self-photosensitization of RhB molecules, which is illustrated in Fig. 9.

In addition, fraction 3 of CDs was employed in the degradation of PNP, one of the most hazardous organic pollutants. To avoid the interference of self-degradation of PNP caused by the UV light, a > 420 nm cut off filter was applied to allow only visible light irradiation of the PNP aqueous sample in presence of the 2-nm CDs. Under the visible light irradiation, no significant degradation of PNP was noticed in absence of the CDs (Fig. S7a). However, the degradation of PNP in presence of the 2-nm CDs occurred shown in Fig. 10a and the degradation rate constant was 2.16×10^{-3}, which was measured based on Fig. 10b. It is noteworthy that the PNP displayed red shift from 313 to 402 nm upon mixing with the 2-nm CDs. This was attributed to the change in the pH from 7.5 to 9.5 that was measured after adding the CDs. Therefore, the rate constant was calculated using the absorbance at 402 nm. Furthermore, Fig. 10b demonstrated that within 150 min, PNP only degraded 30% and the reason is the same as the result shown in Fig. 6b. However, upon the removal of the filter to utilize the full spectrum including UV light, within the same time, PNP degraded by 70% (Fig. S7b) and the rate constant can be enhanced up to 6.17×10^{-3}.

3.3. Photocatalyst stability test

Fraction 3 was tested for its stability after the dye degradation lasted for 150 min. In order to completely remove the residues of RhB, the same solution containing fraction 3 was exposed to the solar simulator for 1 h. Subsequently, we added another fresh 20 μL of RhB to the solution, which was irradiated by the solar simulator. The UV/vis spectrum was recorded each 30 min until the peak at 554 nm disappeared. The whole process was repeated four times. Fig. 11 shows the degradation of RhB over time. There is no significant decrease in the photocatalytic activity of the CDs of fraction 3 and can be reused for another degradation cycle, which reveals good stability. After four cycles of the dye degradation experiment, fraction 3 was characterized by UV/vis and fluorescence spectroscopy. The results were presented in the supporting information as Fig. S8. We observe no obvious differences in activity after multiple uses of the photocatalyst, which again confirms the stability of fraction 3 as the photocatalyst.

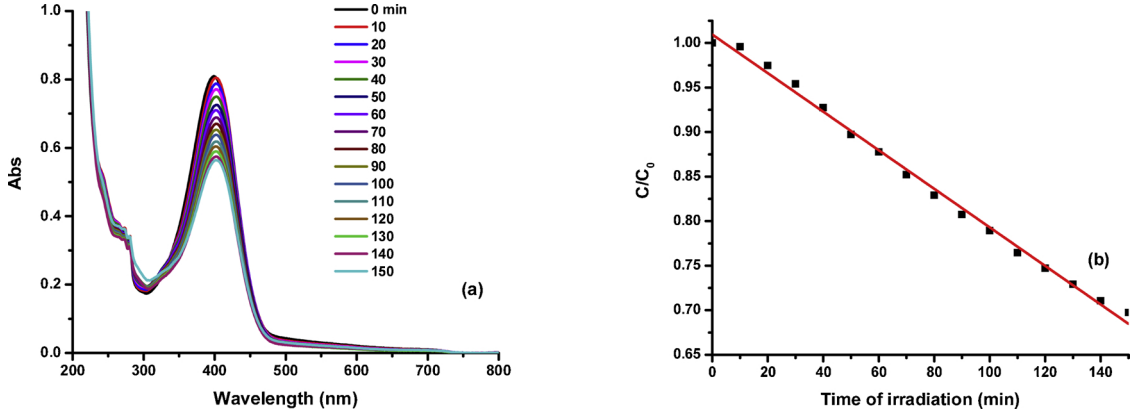

Fig. 10. (a) PNP degradation in presence of CDs (fraction 3) using the filter; (b) the measurement of degradation reaction rate constant. The concentration of fraction 3 is 0.75 mg/mL.

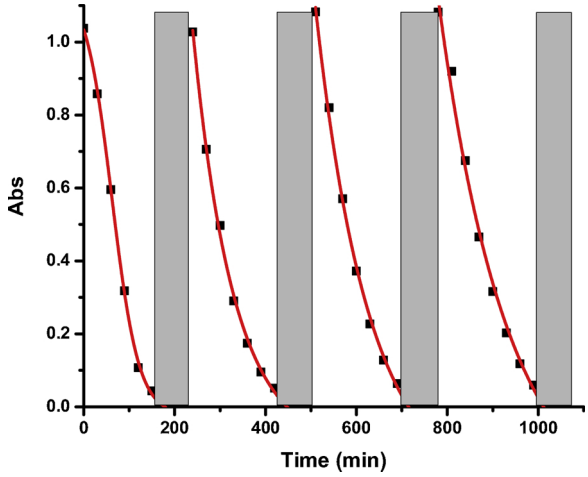

Fig. 11. The stability test of fraction 3 with RhB degradation over time. The grey square represents 1 h of exposure to sunlight. The concentration of fraction 3 is 0.75 mg/mL.

4. Conclusions

A microwave-assisted approach was adopted to create tunable sized CDs that showed unique photoluminescence (PL) behavior, structural properties, and photocatalytic activity and stability. However, there was not a trend between size of CDs and the PL color (wavelength). This shows the PL mechanism of CDs cannot be explained by quantum confinement. The diffuse reflectance spectroscopy analysis indicated semiconductor (fraction 3) properties with a narrow band gap of 2.04 eV. The size of the CDs demonstrated significant effect on their photocatalytic activity in the degradation of organic dyes. The 2-nm CDs showed substantial degradation of RhB and MB under simulated sunlight irradiation. The mechanism of the dye degradation was analyzed using sacrificial scavengers and argon protection, separately. We observed the photocatalytic dye degradation catalyzed by the 2-nm CDs is mainly attributed to the oxidation of the dye by the holes and superoxide radical anions. Fraction 3 was applied to degrade other organic pollutants such as p-nitrophenol and it showed 70% degradation upon irradiation by full spectrum. Also, fraction 3 demonstrated good stability as a photocatalyst for multiple cycles of dye degradation. The study, for the first time, reports a size-dependent photocatalytic dye degradation of CDs, showing a comparable result to those of many metal-containing photocatalysts. These results show the potential of bare CDs with smaller sizes as excellent photocatalysts for pollutant degradation, important for future environmental protection.

Acknowledgments

We gratefully acknowledge the support of the National Science Foundation under Grant 011298 and National Institute of Health under Grant 009887. Elsayed M. Zahran acknowledge support from Ball State University.

Appendix A. Supplementary data

Supplementary material related to this article can be found, in the online version, at doi:https://doi.org/10.1016/j.apcatb.2019.02.019.

References

[1] M. Valenti, E. Kontoleta, I.A. Digdaya, M.P. Jonsson, G. Biskos, A. Schmidt-ott, W.A. Smith, The role of size and dimerization of decorating plasmonic silver nanoparticles on the photoelectrochemical solar water splitting performance of $BiVO_4$ photoanodes, ChemNanoMat 2 (2016) 739–747.
[2] D. Rajamanickam, M. Shanthi, Photocatalytic degradation of an organic pollutant by zinc oxide – solar process, Arab. J. Chem. 9 (2016) S1858–S1868.
[3] A. Fujishima, K. Honda, Electrochemical photolysis of water at a semiconductor electrode, Nature 238 (1972) 37–38.
[4] M. Haro, R. Abargues, I. Herraiz-Cardona, J. Martínez-Pastor, S. Giménez, Plasmonic versus catalytic effect of gold nanoparticles on mesoporous TiO_2 electrodes for water splitting, Electrochim. Acta 144 (2014) 64–70.
[5] W.-H. Hung, T.-M. Chien, C.-M. Tseng, Enhanced photocatalytic water splitting by plasmonic TiO_2–Fe_2O_3 cocatalyst under visible light irradiation, J. Phys. Chem. C 118 (2014) 12676–12681.
[6] X. Chen, Z. Wu, D. Liu, Z. Gao, Preparation of ZnO photocatalyst for the efficient and rapid photocatalytic degradation of Azo dyes, Nanoscale Res. Lett. 12 (2017) 143–152.
[7] J. Wang, Y.-F. Lim, G. Wei Ho, Carbon-ensemble-manipulated ZnS heterostructures for enhanced photocatalytic H_2 evolution, Nanoscale 6 (2014) 9673–9680.
[8] T. Saison, N. Chemin, C. Chanéac, O. Durupthy, L. Mariey, F. Maugé, V. Brezová, J.-P. Jolivet, New insights into $BiVO_4$ properties as visible light photocatalyst, J. Phys. Chem. C 119 (2015) 12967–12977.
[9] G.-S. Li, D.-Q. Zhang, J.C. Yu, A new visible-light photocatalyst: CdS quantum dots embedded mesoporous TiO_2, Environ. Sci. Technol. 43 (2009) 7079–7085.
[10] A. Naseri, M. Samadi, A. Pourjavadi, A.Z. Moshfegh, S. Ramakrishna, Graphitic carbon nitride (g-C_3N_4)-based photocatalysts for solar hydrogen generation: recent advances and future development directions, J. Mater. Chem. A Mater. Energy Sustain. 5 (2017) 23406–23433.
[11] M. Sachsenhauser, K. Walczak, P.A. Hampel, M. Stutzmann, I.D. Sharp, J.A. Garrido, Suppression of photoanodic surface oxidation of n-type 6H-SiC electrodes in aqueous electrolytes, Langmuir 32 (2016) 1637–1644.
[12] T. Jafari, E. Moharreri, A. Amin, R. Miao, W. Song, S. Suib, Photocatalytic water splitting—the untamed dream: a review of recent advances, Molecules 21 (2016) 900–928.
[13] B. Wang, S. Wang, Y. Wang, Y. Lv, H. Wu, X. Ma, M. Tan, Highly fluorescent carbon dots for visible sensing of doxorubicin release based on efficient nanosurface energy transfer, Biotechnol. Lett. 38 (2016) 191–201.
[14] Y. Zhou, A. Desserre, S.K. Sharma, S. Li, M.H. Marksberry, C.C. Chusuei, P.L. Blackwelder, R.M. Leblanc, Gel-like carbon dots: characterization and their potential applications, ChemPhysChem 18 (2017) 890–897.
[15] X. Wang, K. Qu, B. Xu, J. Ren, X. Qu, Microwave assisted one-step green synthesis of cell-permeable multicolor photoluminescent carbon dots without surface passivation reagents, J. Mater. Chem. 21 (2011) 2445–2450.
[16] Y.-P. Sun, B. Zhou, Y. Lin, W. Wang, K.A.S. Fernando, P. Pathak, M.J. Meziani, B.A. Harruff, X. Wang, H. Wang, P.G. Luo, H. Yang, M.E. Kose, B. Chen, L.M. Veca, S.-Y. Xie, Quantum-sized carbon dots for bright and colorful photoluminescence, J. Am. Chem. Soc. 128 (2006) 7756–7757.
[17] Z. Ma, H. Ming, H. Huang, Y. Liu, Z. Kang, One-step ultrasonic synthesis of fluorescent N-doped carbon dots from glucose and their visible-light sensitive photocatalytic ability, New J. Chem. 36 (2012) 861–864.
[18] Y. Wang, A. Hu, Carbon quantum dots: synthesis, properties and applications, J. Mater. Chem. C Mater. Opt. Electron. Devices 2 (2014) 6921–6939.
[19] Y. Zhou, K. Mintz, C. Oztan, S. Hettiarachchi, Z. Peng, E. Seven, P. Liyanage, S. De La Torre, E. Celik, R. Leblanc, Embedding carbon dots in superabsorbent polymers for additive manufacturing, Polymers 10 (2018) 921–932.
[20] Y. Zhou, Z. Peng, E.S. Seven, R.M. Leblanc, Crossing the blood-brain barrier with nanoparticles, J. Control. Release 270 (2018) 290–303.
[21] K.J. Mintz, G. Mercado, Y. Zhou, Y. Ji, S.D. Hettiarachchi, P.Y. Liyanage, R.R. Pandey, C.C. Chusuei, J. Dallman, R.M. Leblanc, Tryptophan carbon dots and their ability to cross the blood-brain barrier, Colloids Surf. B Biointerfaces 176 (2019) 488–493.
[22] Y. Song, S. Zhu, B. Yang, Bioimaging based on fluorescent carbon dots, RSC Adv. 4 (2014) 27184–27200.
[23] Z. Peng, E.H. Miyanji, Y. Zhou, J. Pardo, S.D. Hettiarachchi, S. Li, P.L. Blackwelder, I. Skromne, R.M. Leblanc, Carbon dots: promising biomaterials for bone-specific imaging and drug delivery, Nanoscale 9 (2017) 17533–17543.
[24] B.B. Campos, R. Contreras-Cáceres, T.J. Bandosz, J. Jiménez-Jiménez, E. Rodríguez-Castellón, J.C.G. Esteves da Silva, M. Algarra, Carbon dots as fluorescent sensor for detection of explosive nitrocompounds, Carbon 106 (2016) 171–178.
[25] K. Mintz, E. Waidely, Y. Zhou, Z. Peng, A.O. Al-Youbi, A.S. Bashammakh, M.S. El-Shahawi, R.M. Leblanc, Carbon dots and gold nanoparticles based immunoassay for detection of alpha-L-fucosidase, Anal. Chim. Acta 1041 (2018) 114–121.
[26] Z. Zhijie, Z. Tingting, L. Xiaoming, X. Jiayue, Z. Haibo, Progress of carbon quantum dots in photocatalysis applications, Part. Part. Syst. Charact. 33 (2016) 457–472.
[27] L. Cao, S. Sahu, P. Anilkumar, C.E. Bunker, J. Xu, K.A.S. Fernando, P. Wang, E.A. Guliants, K.N. Tackett, Y.-P. Sun, Carbon nanoparticles as visible-light photocatalysts for efficient CO_2 conversion and beyond, J. Am. Chem. Soc. 133 (2011) 4754–4757.
[28] J. Wang, Y.H. Ng, Y.-F. Lim, G.W. Ho, Vegetable-extracted carbon dots and their nanocomposites for enhanced photocatalytic H_2 production, RSC Adv. 4 (2014) 44117–44123.
[29] E. Celik, C. Oztan, Y. Zhou, R. LeBlanc, O. Genc, S. Ballikaya, Enhancement of Thermoelectric Figure of Merit of Bi_2Te_3 Using Carbon Dots, (2018) V06BT08A039.
[30] S. Sahu, B. Behera, T.K. Maiti, S. Mohapatra, Simple one-step synthesis of highly luminescent carbon dots from orange juice: application as excellent bio-imaging agents, Chem. Commun. 48 (2012) 8835–8837.
[31] A. Chae, Y. Choi, S. Jo, P. Nur'aeni, S.Y. Paoprasert, I. Park, Microwave-assisted synthesis of fluorescent carbon quantum dots from an A2/B3 monomer set, RSC Adv. 7 (2017) 12663–12669.
[32] C. Zheng, X. An, J. Gong, Novel pH sensitive N-doped carbon dots with both long fluorescence lifetime and high quantum yield, RSC Adv. 5 (2015) 32319–32322.

[33] J. Rodrigues, S.O. Pereira, S. Soreto Teixeira, Y. Zhou, Z. Peng, P.Y. Liyanage, R.M. Leblanc, A.M.M.V. Barros-Timmons, L.C. Costa, F.M. Costa, T. Monteiro, Insights into the photoluminescence properties of gel-like carbon quantum dots embedded in poly(methyl methacrylate) polymer, Mater. Today Comm. 18 (2019) 32–38.
[34] S. Zhu, Y. Song, X. Zhao, J. Shao, J. Zhang, B. Yang, The photoluminescence mechanism in carbon dots (graphene quantum dots, carbon nanodots, and polymer dots): current state and future perspective, Nano Res. 8 (2015) 355–381.
[35] L. Han, S.G. Liu, J.X. Dong, J.Y. Liang, L.J. Li, N.B. Li, H.Q. Luo, Facile synthesis of multicolor photoluminescent polymer carbon dots with surface-state energy gap-controlled emission, J. Mater. Chem. C 5 (2017) 10785–10793.
[36] K. Takanabe, Photocatalytic water splitting: quantitative approaches toward photocatalyst by design, ACS Catal. 7 (2017) 8006–8022.
[37] J. Yu, C. Liu, K. Yuan, Z. Lu, Y. Cheng, L. Li, X. Zhang, P. Jin, F. Meng, H. Liu, Luminescence mechanism of carbon dots by tailoring functional groups for sensing Fe^{3+} ions, Nanomaterials 8 (2018) 233–244.
[38] X. Li, S. Zhang, S.A. Kulinich, Y. Liu, H. Zeng, Engineering surface states of carbon dots to achieve controllable luminescence for solid-luminescent composites and sensitive Be^{2+} detection, Sci. Rep. 4 (2014) 4976–4983.
[39] F. Yuan, Z. Wang, X. Li, Y. Li, Za. Tan, L. Fan, S. Yang, Bright multicolor bandgap fluorescent carbon quantum dots for electroluminescent light-Emitting diodes, Adv. Mater. 29 (2017) 1604436–1604441.
[40] M. Reza Gholipour, C.-T. Dinh, F. Beland, T.-O. Do, Nanocomposite heterojunctions as sunlight-driven photocatalysts for hydrogen production from water splitting, Nanoscale 7 (2015) 8187–8208.
[41] D.-W. Zheng, B. Li, C.-X. Li, J.-X. Fan, Q. Lei, C. Li, Z. Xu, X.-Z. Zhang, Carbon-dot-decorated carbon nitride nanoparticles for enhanced photodynamic therapy against hypoxic tumor via water splitting, ACS Nano 10 (2016) 8715–8722.
[42] M. Ni, M.K.H. Leung, D.Y.C. Leung, K. Sumathy, A review and recent developments in photocatalytic water-splitting using TiO_2 for hydrogen production, Renew. Sustain. Energy Rev. 11 (2007) 401–425.
[43] X. Wang, K. Maeda, A. Thomas, K. Takanabe, G. Xin, J.M. Carlsson, K. Domen, M. Antonietti, A metal-free polymeric photocatalyst for hydrogen production from water under visible light, Nat. Mater. 8 (2008) 76–80.
[44] R. Wang, K.-Q. Lu, F. Zhang, Z.-R. Tang, Y.-J. Xu, 3D carbon quantum dots/graphene aerogel as a metal-free catalyst for enhanced photosensitization efficiency, Appl. Catal. B 233 (2018) 11–18.
[45] N. Zhang, M.-Q. Yang, S. Liu, Y. Sun, Y.-J. Xu, Waltzing with the versatile platform of graphene to synthesize composite photocatalysts, Chem. Rev. 115 (2015) 10307–10377.
[46] K.-Q. Lu, Q. Quan, N. Zhang, Y.-J. Xu, Multifarious roles of carbon quantum dots in heterogeneous photocatalysis, J. Energy Chem. 25 (2016) 927–935.
[47] R. Wang, K.-Q. Lu, Z.-R. Tang, Y.-J. Xu, Recent progress in carbon quantum dots: synthesis, properties and applications in photocatalysis, J. Mater. Chem. A Mater. Energy Sustain. 5 (2017) 3717–3734.
[48] H. Liu, Z. Li, Y. Sun, X. Geng, Y. Hu, H. Meng, J. Ge, L. Qu, Synthesis of luminescent carbon dots with ultrahigh quantum yield and inherent folate receptor-positive cancer cell targetability, Sci. Rep. 8 (2018) 1086–1093.
[49] H. Zhang, H. Ming, S. Lian, H. Huang, H. Li, L. Zhang, Y. Liu, Z. Kang, S.-T. Lee, Fe_2O_3/carbon quantum dots complex photocatalysts and their enhanced photocatalytic activity under visible light, Dalton Trans. 40 (2011) 10822–10825.
[50] H. Yu, Y. Zhao, C. Zhou, L. Shang, Y. Peng, Y. Cao, L.-Z. Wu, C.-H. Tung, T. Zhang, Carbon quantum dots/TiO2 composites for efficient photocatalytic hydrogen evolution, J. Mater. Chem. A 2 (2014) 3344–3351.
[51] S. Muthulingam, K.B. Bae, R. Khan, I.-H. Lee, P. Uthirakumar, Carbon quantum dots decorated N-doped ZnO: synthesis and enhanced photocatalytic activity on UV, visible and daylight sources with suppressed photocorrosion, J. Environ. Chem. Eng. 4 (2016) 1148–1155.
[52] Z. Cheng, F. Wang, T.A. Shifa, K. Liu, Y. Huang, Q. Liu, C. Jiang, J. He, Carbon dots decorated vertical SnS2 nanosheets for efficient photocatalytic oxygen evolution, Appl. Phys. Lett. 109 (2016) 053905–053909.
[53] Y. Zhang, M. Park, H.Y. Kim, B. Ding, S.-J. Park, A facile ultrasonic-assisted fabrication of nitrogen-doped carbon dots/BiOBr up-conversion nanocomposites for visible light photocatalytic enhancements, Sci. Rep. 7 (2017) 45086–45097.
[54] P. Yang, J. Zhao, L. Zhang, L. Li, Z. Zhu, Intramolecular hydrogen bonds quench photoluminescence and enhance photocatalytic activity of carbon nanodots, Chem. Eur. J. 21 (2015) 8561–8568.
[55] L. Haitao, H. Xiaodie, K. Zhenhui, H. Hui, L. Yang, L. Jinglin, L. Suoyuan, Chi Him A. Tsang, Y. Xiaobao, L. Shuit-Tong, Water-soluble fluorescent carbon quantum dots and photocatalyst design, Angew. Chem. Int. Ed. 49 (2010) 4430–4434.
[56] Y. Chen, F. Sun, Z. Huang, H. Chen, Z. Zhuang, Z. Pan, J. Long, F. Gu, Photochemical fabrication of SnO_2 dense layers on reduced graphene oxide sheets for application in photocatalytic degradation of p-nitrophenol, Appl. Catal. B 215 (2017) 8–17.
[57] Z. Gao, X. Wang, J. Chang, D. Wu, L. Wang, X. Liu, F. Xu, Y. Guo, K. Jiang, Fluorescent carbon quantum dots, capacitance and catalysis active porous carbon microspheres from beer, RSC Adv. 5 (2015) 48665–48674.
[58] Z. Yiqun, P.Y. Liyanage, D.L. Geleroff, Z. Peng, K.J. Mintz, S.D. Hettiarachchi, R.R. Pandey, C.C. Chusuei, P.L. Blackwelder, R.M. Leblanc, Photoluminescent carbon dots: a mixture of heterogeneous fractions, ChemPhysChem 19 (2018) 1–10.
[59] A.C. Vandaele, C. Hermans, P.C. Simon, M. Van Roozendael, J.M. Guilmot, M. Carleer, R. Colin, Fourier transform measurement of NO_2 absorption cross-section in the visible range at room temperature, J. Atmos. Chem. 25 (1996) 289–305.
[60] D. Zhou, D. Li, P. Jing, Y. Zhai, D. Shen, S. Qu, A.L. Rogach, Conquering aggregation-induced solid-state luminescence quenching of carbon dots through a carbon dots-triggered silica gelation process, Chem. Mater. 29 (2017) 1779–1787.
[61] S. Nag, D.J. Begley, Blood-brain barrier, exchange of metabolites and gases, in: H. Kalimo (Ed.), Cerebrovascular Diseases, ISN Neuropath Press, Basel, 2005, pp. 22–29.
[62] Y. Tooru, An x-ray photoelectron spectroscopic study of several ligands in coordination compounds, Bull. Chem. Soc. Jpn. 53 (1980) 1327–1330.
[63] C.D. Wagner, D.A. Zatko, R.H. Raymond, Use of the oxygen KLL Auger lines in identification of surface chemical states by electron spectroscopy for chemical analysis, Anal. Chem. 52 (1980) 1445–1451.
[64] High resolution XPS of organic polymers: the scienta ESCA300 database (Beamson, G.; Briggs, D.), J. Chem. Educ. 70 (1993) A25.
[65] S. Hu, R. Tian, L. Wu, Q. Zhao, J. Yang, J. Liu, S. Cao, Chemical regulation of carbon quantum dots from synthesis to photocatalytic activity, Asian J. Chem. 8 (2013) 1035–1041.
[66] M. Han, S. Zhu, S. Lu, Y. Song, T. Feng, S. Tao, J. Liu, B. Yang, Recent progress on the photocatalysis of carbon dots: classification, mechanism and applications, Nano Today 19 (2018) 201–218.
[67] Y.-Q. Zhang, D.-K. Ma, Y.-G. Zhang, W. Chen, S.-M. Huang, N-doped carbon quantum dots for TiO2-based photocatalysts and dye-sensitized solar cells, Nano Energy 2 (2013) 545–552.
[68] M. Pálmai, E.M. Zahran, S. Angaramo, S. Bálint, Z. Pászti, M.R. Knecht, L.G. Bachas, Pd-decorated m-$BiVO_4$/BiOBr ternary composite with dual heterojunction for enhanced photocatalytic activity, J. Mater. Chem. A 5 (2017) 529–534.
[69] Y. Zhang, N. Zhang, Z.-R. Tang, Y.-J. Xu, Identification of Bi_2WO_6 as a highly selective visible-light photocatalyst toward oxidation of glycerol to dihydroxyacetone in water, Chem. Sci. 4 (2013) 1820–1824.
[70] L. Yuan, M.-Q. Yang, Y.-J. Xu, Tuning the surface charge of graphene for self-assembly synthesis of a $SnNb_2O_6$ nanosheet–graphene (2D–2D) nanocomposite with enhanced visible light photoactivity, Nanoscale 6 (2014) 6335–6345.